

Limpet Tooth-Inspired Painless Microneedles Fabricated by Magnetic Field-Assisted 3D Printing

Xiangjia Li,* Weitong Shan, Yang Yang, Dylan Joralmon, Yizhen Zhu, Yiyu Chen, Yuan Yuan, Han Xu, Jiahui Rong, Rui Dai, Qiong Nian, Yang Chai,* and Yong Chen*

Microneedle arrays show many advantages in drug delivery applications due to their convenience and reduced risk of infection. Compared to other microscale manufacturing methods, 3D printing easily overcomes challenges in the fabrication of microneedles with complex geometric shapes and multifunctional performance. However, due to material characteristics and limitations on printing capability, there are still bottlenecks to overcome for 3D printed microneedles to achieve the mechanical performance needed for various clinical applications. The hierarchical structures in limpet teeth, which are extraordinarily strong, result from aligned fibers of mineralized tissue and protein-based polymer reinforced frameworks. These structures provide design inspiration for mechanically reinforced biomedical microneedles. Here, a bioinspired microneedle array is fabricated using magnetic field-assisted 3D printing (MF-3DP). Micro-bundles of aligned iron oxide nanoparticles (aIOs) are encapsulated by polymer matrix during the printing process. A bioinspired 3D-printed painless microneedle array is fabricated, and suitability of this microneedle patch for drug delivery during long-term wear is demonstrated. The results reported here provide insights into how the geometrical morphology of microneedles can be optimized for the painless drug delivery in clinical trials.

pain. These needles generate copious amounts of medical waste and can only be used with formal medical training.^[1] To overcome these shortcomings, a novel medical instrument called a microneedle (MN) patch was developed, and this technology is ultimately expected to largely replace hypodermic needles in medical settings.^[1] MN arrays have a number of notable strengths, for example, operational convenience, reduced pain, compatibility with many drugs, low infection rate, multiple drug carriage capability, etc.^[2–7] Among microfabrication technologies, 3D printing shows great promise for fabricating MNs with diverse geometric shapes for different functionalities.^[5,8–11] However, it remains a challenge to use 3D printing technologies, such as fused deposition modeling (FDM), inkjet printing, and selective laser sintering, to fabricate microscale MNs with fine detail to the necessary degree of precision.^[12–18] Thus, current 3D-printed MNs largely rely on

1. Introduction

Hypodermic needles have been widely used in medicine for over a hundred and fifty years due to their low cost and ability to inject a large volume of fluid. However, the insertion of hypodermic needles is usually accompanied by intense

additional processing procedures, typically chemical etching, to further reduce the feature size and sharpen or refine the features. Nonetheless, the micro-features of MNs remain difficult to control precisely using post-processing.^[8] Several approaches have been taken to design and fabricate MNs using micro-scale 3D printing processes, such as micro-scale

Prof. X. Li, D. Joralmon, Y. Zhu, R. Dai, Prof. Q. Nian
Department of Aerospace and Mechanical Engineering
School for Engineering of Matter
Transport and Energy
Arizona State University
501 E. Tyler Mall, Tempe, AZ 85287, USA
E-mail: xiangjia.li@asu.edu


W. Shan
Mork Family Department of Chemical Engineering & Materials Science
Viterbi School of Engineering
University of Southern California
925 Bloom Walk, Los Angeles, CA 90089, USA

Prof. Y. Yang
Department of Mechanical Engineering
San Diego State University
5500 Campanile Drive, San Diego, CA 92182, USA

Y. Chen, J. Rong, Prof. Y. Chen
Department of Aerospace and Mechanical Engineering
Viterbi School of Engineering
University of Southern California
3650 McClintock Ave, Los Angeles, CA 90089, USA
E-mail: yongchen@usc.edu

Dr. Y. Yuan, Prof. Y. Chai
Center for Craniofacial Molecular Biology
University of Southern California
2250 Alcazar St, Los Angeles, CA 90089, USA
E-mail: ychai@usc.edu

H. Xu, Prof. Y. Chen
Epstein Department of Industrial and Systems Engineering
University of Southern California
3715 McClintock Ave, Los Angeles, CA 90089, USA

 The ORCID identification number(s) for the author(s) of this article can be found under <https://doi.org/10.1002/adfm.202003725>.

DOI: 10.1002/adfm.202003725

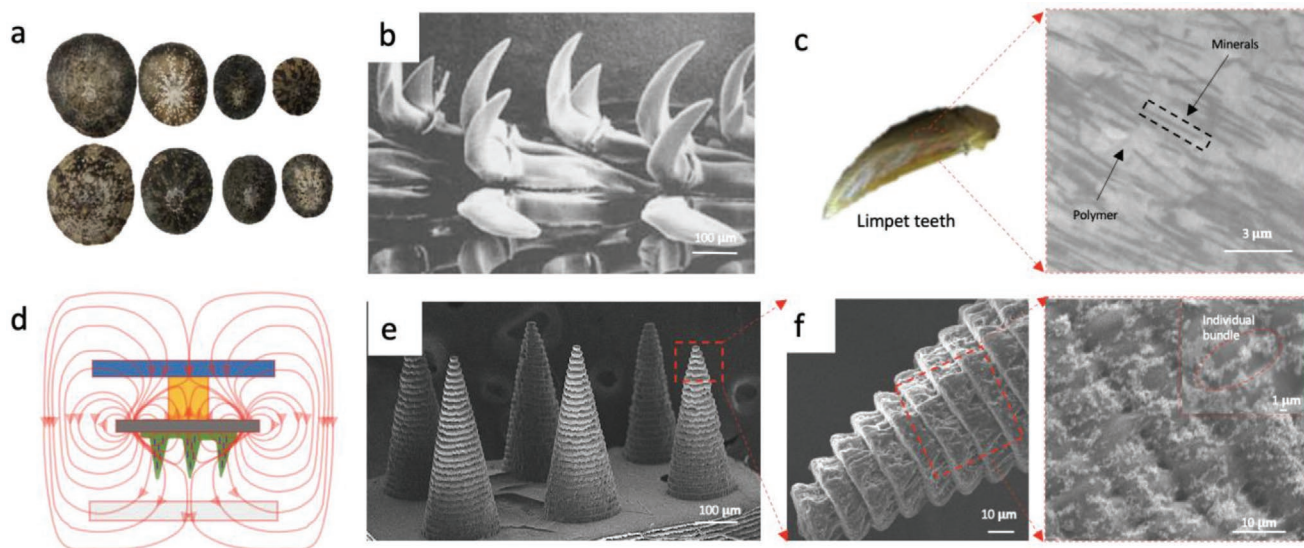


Figure 1. Limpet tooth-inspired 3D-printed MN array. a) Limpet shell; b) micro-scale limpet teeth (Reproduced with permission.^[20] Copyright 2015, Royal Society); c) cross-sectional view of a limpet tooth with aligned mineral fibers (Reproduced with permission.^[20] Copyright 2015, Royal Society); d) schematic diagram of fabrication of limpet tooth-inspired MN array using the MF-3DP process; e) scanning electron microscope (SEM) images of MF-3D-printed MN array; and f) magnification of one MF-3D-printed MN with aIOs.

stereolithography and two-photon polymerization.^[12–15] Even though more complex shapes of MNs have been successfully produced using these techniques, the poor mechanical performance of each individual needle remains a major issue.^[13,14,16] The overall size of each needle has to be relatively large to provide sufficient strength, but the enlarged size also increases pain during insertion.^[14,15] Weak mechanical performance of 3D printed MNs is therefore a bottleneck that hinders their applications in the clinic.^[19]

In nature, some creatures have tissues that exhibit remarkable mechanical properties attributed to their unique microstructures and biomaterials.^[20–22] For example, brick-and-mortar-shaped structures in nacre and bouligand-type structures in lobster claws demonstrate excellent mechanical performance.^[21,22] Recently, scientists revealed that the teeth of limpets (**Figure 1a**), which are shelled aquatic snails that adhere themselves to rocks, may be the strongest material found in nature.^[20] The extreme mechanical strength of tiny limpet teeth (**Figure 1b**) results from their distinctive hierarchical structures, in which high numbers of goethite nanofibers are arranged parallel to the surface (**Figure 1c**).^[20] 3D printing has created new opportunities for manipulating and fabricating such multi-scale, multi-material, and multi-functional structures by providing superior control over the formation of geometric shapes.^[23–25] The unique ability of 3D printing to create biomimetic structures opens the door to new possibilities for the fabrication and processing of MNs with improved mechanical performance.

In this work, MNs were designed with inspiration from limpet teeth, and fabricated with reinforced iron oxide particle (IO)-based nanofillers for painless injection. A magnetic field assisted 3D printing (MF-3DP) process was developed to build these MNs using aligned iron oxide nanoparticles (aIOs) and polymer matrix material. The hierarchical structures of limpet teeth were successfully reproduced through the

MF-3DP process to achieve extremely strong MNs (**Figure 1d**). This fabrication procedure achieved precise micro-filler alignment via magnetic control. Through selective crosslinking of the photocurable polymer, the aligned nanoparticle bundles were encapsulated inside the printed MNs using the MF-3DP process (**Figure 1e,f**). The 3D-printed hierarchical structures with aIOs showed enhanced mechanical properties compared to those with random iron oxide nanoparticles (rIOs). The limpet tooth-inspired architecture enhanced the mechanical strength through aligning IOs in each layer to maximize their performance.

The MF-3DP process demonstrated the ability to fabricate 3D microstructures with outstanding mechanical performance. The MNs printed using the MF-3DP process were able to overcome the drawbacks of MNs made using traditional manufacturing methods. For example, patients usually feel intense discomfort during insertion of hypodermic needles for allergy testing or vaccine administration.^[26] The magnetic field assisted 3D printed (MF-3D-printed) MNs benefited from having smaller dimensions and sharp tips, thus requiring less insertion force when applied, reducing potential contact area with pain-sensing neurons and therefore minimizing pain. Also, the MF-3D-printed MNs may provide a solution to control over vaccine administration to the epidermal and dermal layers of the skin by enabling accurate deposition depth, which is difficult to achieve with traditional drug delivery technologies.^[27] Moreover, experiments showed that mice administered with an MF-3D-printed MN patch did not feel its existence at all, while the MNs remained in the same location over a long period of time, even when the mice moved vigorously. Our in vivo results therefore indicate that the MF-3D-printed MN array possesses the potential for long-term drug delivery in animals and humans. Overall, we demonstrate that the newly developed MF-3DP process enabled the fabrication of MNs with greatly improved mechanical performance for predictable

drug delivery, and also successfully achieved several important performance targets, such as painless insertion and ease of use for practitioners.

2. Results and Discussion

2.1. MF-3DP of Limpet Tooth-Inspired MNs

As mentioned above, limpet teeth demonstrate incredible mechanical performance due to their hierarchical, fiber-reinforced composition, and nanoscale effect and interface.^[20] The strong anisotropy of limpet teeth owes to the alignment of goethite-based mineral fibers, each of which is approximately 3 μm long and 20 nm in diameter (Figure 1c). Bio-mimicking such hierarchically organized, mineral fiber-reinforced structures is challenging for traditional nanocomposite printing. Magnetic fields provide a potential solution by enabling the filler to be aligned inside the polymer matrix.^[21,28] The magnetic field-assisted alignment has high dynamic performance in quick response and good robustness compared to the electrically assisted alignment.^[21] For example, the alignment response time of nanoparticles in the electric field-assisted 3D printing will take over 1 min, while it only takes half a second for the nanoparticles to be aligned in the magnetic field.^[22,23] Moreover, the magnetic field-assisted processes have the capability to realize alignment in any spatial directions by applying

specially designed magnetic field, and the magnetic field will lead to the alignment of particles/fibers without the contact of the magnet and the composites, while for the electric field, the electrodes have to be immersed in the composite to work effectively.^[20–33] In this work, a MF-3DP process was developed by integrating a dynamic magnetic field with microscale mask image projection-based stereolithography (Figure 2a). In this process, a controllable magnetic field was applied in the printing region, which was filled with photocurable composite material. Combining dynamic control of the magnetic field with the projection of a 2D light beam, microscale structures with special alignment of magnetic particles could be constructed by selectively curing the photocurable composite material (Figure 2b). As shown in Figure 2c, the alignment directions of the magnetic particles were changed along with the orientation of the magnetic field. Furthermore, the diameters of the assembled magnetic bundles and the width of the gaps between them were modulated by adjusting the magnetic particle concentration within the photocurable composite material (see in Figure 2d).

In limpet teeth, mineral fibers run parallel to the surface. For this reason, we imposed a cylindrical magnetic field with radius R on the z axis to build the reinforced MNs, such that the alignment of IOs was always parallel to the direction of material accumulation. The magnetic nanoparticles assembled and converged along the magnetic flux in the magnetic field (Figure 2a). The strength of the applied magnetic field B can

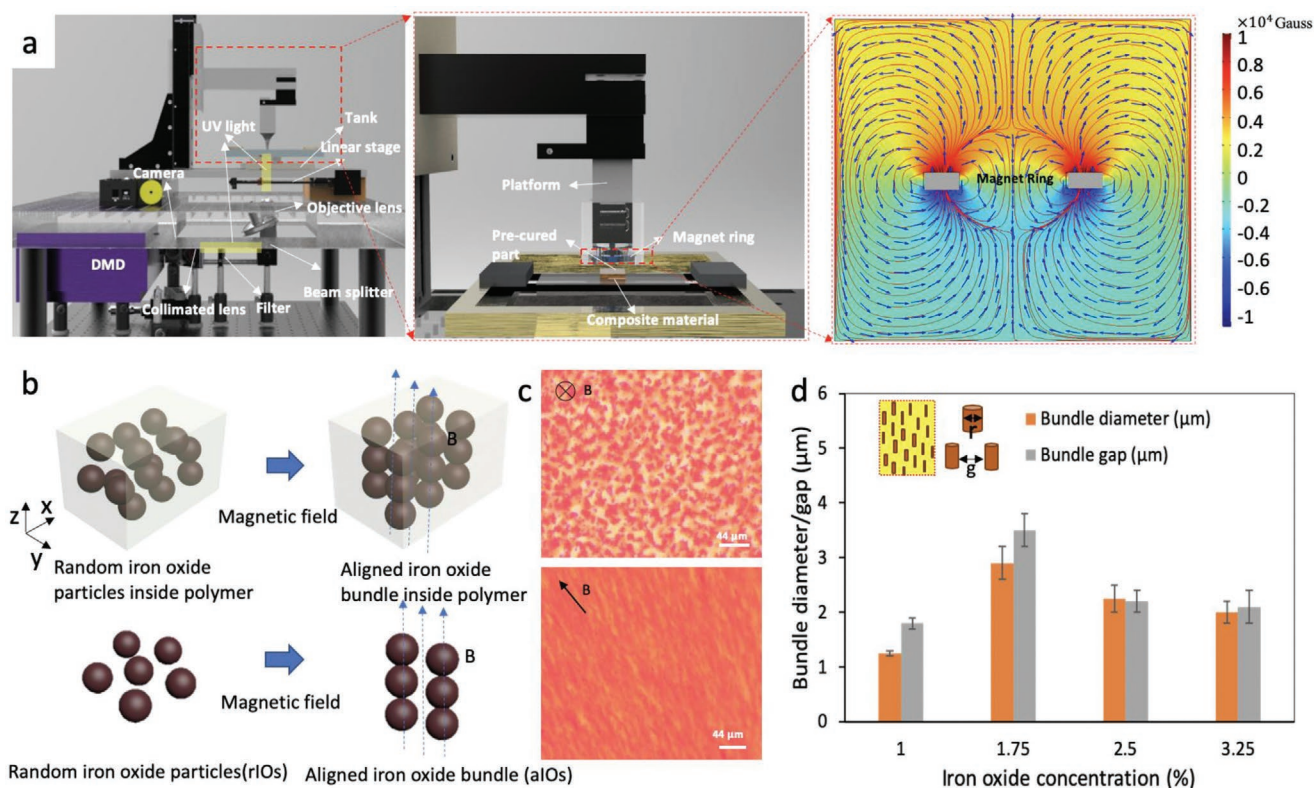


Figure 2. a) Schematic diagram of the MF-3DP process and simulation of the magnetic field applied in the MF-3DP process by COMSOL Multiphysics; b) schematic diagrams showing the alignment of IOs along the printing direction by imposing the magnetic field; c) aligned iron oxide composite in the magnetic field with different magnetic field orientations, and d) diameters and gaps of aIO bundles generated by using IO/polymer composite with different IO concentrations.

be determined through the principle of superposition by the equation:^[34]

$$B(z) = \frac{u_0 M}{2} \left[\frac{z}{\sqrt{z^2 + R_0^2}} - \frac{z-L}{\sqrt{(z-L)^2 + R_0^2}} - \left(\frac{z}{\sqrt{z^2 + R_1^2}} - \frac{z-L}{\sqrt{(z-L)^2 + R_1^2}} \right) \right] \quad (1)$$

where z is the distance from the center of the cylindrical magnetic field, $u_0 = 4\pi \times 10^{-7} \text{ H m}^{-1}$, the cylindrical magnetic field with magnetization $+M$ with radius R_0 , and another half-cylindrical magnetic field with magnetization $-M$ with radius R_1 .

The magnetic field strength is related to the distance H between the printing material and the magnetic field generator (see in Figure S1, Supporting Information). Based on Equation (1), the magnetic field strength decreases, then increases to a peak value, and eventually decreases again (Figure S1b, Supporting Information). The cylindrical magnetic field thus enabled the alignment of IOs in the printing direction, which has proven difficult to achieve using other methods.^[21] In the magnetic field, the magnetic particles escaped from the van der Waals and electro-static forces (see Supporting Information) but aggregated together due to the dominant magnetic force, which can be calculated using:^[35]

$$\vec{F}_{mp} = \mu_f V_p \frac{3(\chi_p - \chi_f)}{[(\chi_p - \chi_f) + 3(\chi_f + 1)]} (\vec{H}_a \cdot \nabla) \vec{H}_a \quad (2)$$

where μ_f is the permeability of the photocurable composite composed of magnetic particles and polymer; χ_p is the ratio of the magnetization of the magnetic particles in the local magnetic field; χ_f is the susceptibility of the photocurable composite; \vec{H}_a is the magnetic field; and V_p is the velocity of the magnetic particles.

A physical experiment was conducted to further investigate the relationship between the geometric shapes of magnetic nanoparticle bundles and the mass concentration of magnetic particles in the polymer composite. Figure 2b showed that the rIOs formed aIO bundles in a direction parallel to the magnetic field orientation. The alignment direction of aIOs bundles could be quickly changed by adjusting the magnetic field orientation (Video S1, Supporting Information). The diameter of the aIO bundles first increased and then decreased as the mass concentration of IOs in the composite increased, and the same trend was also discovered for the width of the gap between each bundle. This is because the diameter of the aIO bundles first grew along with the increase of IOs in the composite material. After the diameter of the IOs reached the saturation point, the bundle diameter stayed the same and the length of the aIO bundles was determined by the layer thickness. Meanwhile, the density of aIO bundles increased along with the mass concentration of IOs, and the gaps between bundles were accordingly reduced.^[36–38] Based on the experimental results, the IO concentration was adjusted to achieve different diameters and densities of the aIO bundles, and their effects on the mechanical performance of the 3D-printed material were assessed. For example, the diameter and gap width of aIO bundles generated using 1.75% (w/w) iron oxide composite in a magnetic field

with a strength of 180 G were 3 μm and 3.5 μm , respectively. The arrangements of IOs in applied magnetic fields with different strengths were also studied, and the results are shown in Figure S1c, Supporting Information. According to the assembly conditions of IOs in a circular magnetic field, the distance H between the printing material and the magnetic field generator was set at 15 mm to achieve a homogenous alignment of IOs along the printing direction.

2.2. Investigation of Curing Characteristics

Limpet tooth-inspired MNs were designed in Solidworks and fabricated using the MF-3DP process (Figure 3a). The IO/polymer composite material was deposited layer by layer to form the MNs. To maintain a uniform density of aIO bundles in the printed material, the IO/polymer composite was refilled after the fabrication of the previous layer, and it only took milliseconds to assemble the aIO bundles in the applied magnetic field. The MNs were arranged in a tetragonal pattern with each conical needle being 200 μm in diameter at its base, and the digital model of the MN array was sliced to create a series of 2D mask projection images. The printing resolution of MF-3DP was influenced by the diameter of the magnetic particles (Figure 3b). This is because the projection light was scattered by the aligned magnetic particles, and there was not enough energy for photocurable polymer to initiate the chemical reaction. Even much bigger and stronger bundles were generated by using the iron-based composite, but it was difficult to fabricate fine features whose sizes were smaller than 10 μm using the iron microparticle-based composite due to the dimensions of the iron bundles (Figure S2, Supporting Information).

In order to fabricate MNs with sharp tips, the curing characteristics of iron- and iron oxide-reinforced composites during the MF-3DP process were studied. The magnetic particles agglomerated and formed micro-scale bundles in the magnetic field, and the projection light was scattered by the magnetic particle bundles, which were homogeneously distributed in the liquid resin. Thus, the light penetration depth of magnetic particle-based composite material was reduced. The curing depth of photocurable material is determined by the light penetration depth and light exposure energy. The relationship between the cure depth C_d and the energy input E_{max} is defined by the Jacob's equation:^[39–41] $C_d = D_p \ln \left(\frac{E_{\text{max}}}{E_c} \right)$ where E_c is the critical energy density, that is, the minimum energy for the photocurable resin to be solidified; and D_p is the light penetration depth. In MF-3DP, the cure depth of the magnetic particle-reinforced composite material C_d can be determined by the following equation:^[41,42]

$$C_d = \frac{D_p}{1 + \frac{3w\rho'D_p}{4a \left(100 - \left(1 - \frac{\rho'}{\rho} \right) w \right) \rho}} \ln \frac{\sqrt{\pi} I_0 R}{E_c} \quad (3)$$

where w is the concentration of the magnetic particles in the composite material; a is the diameter of the magnetic particles;

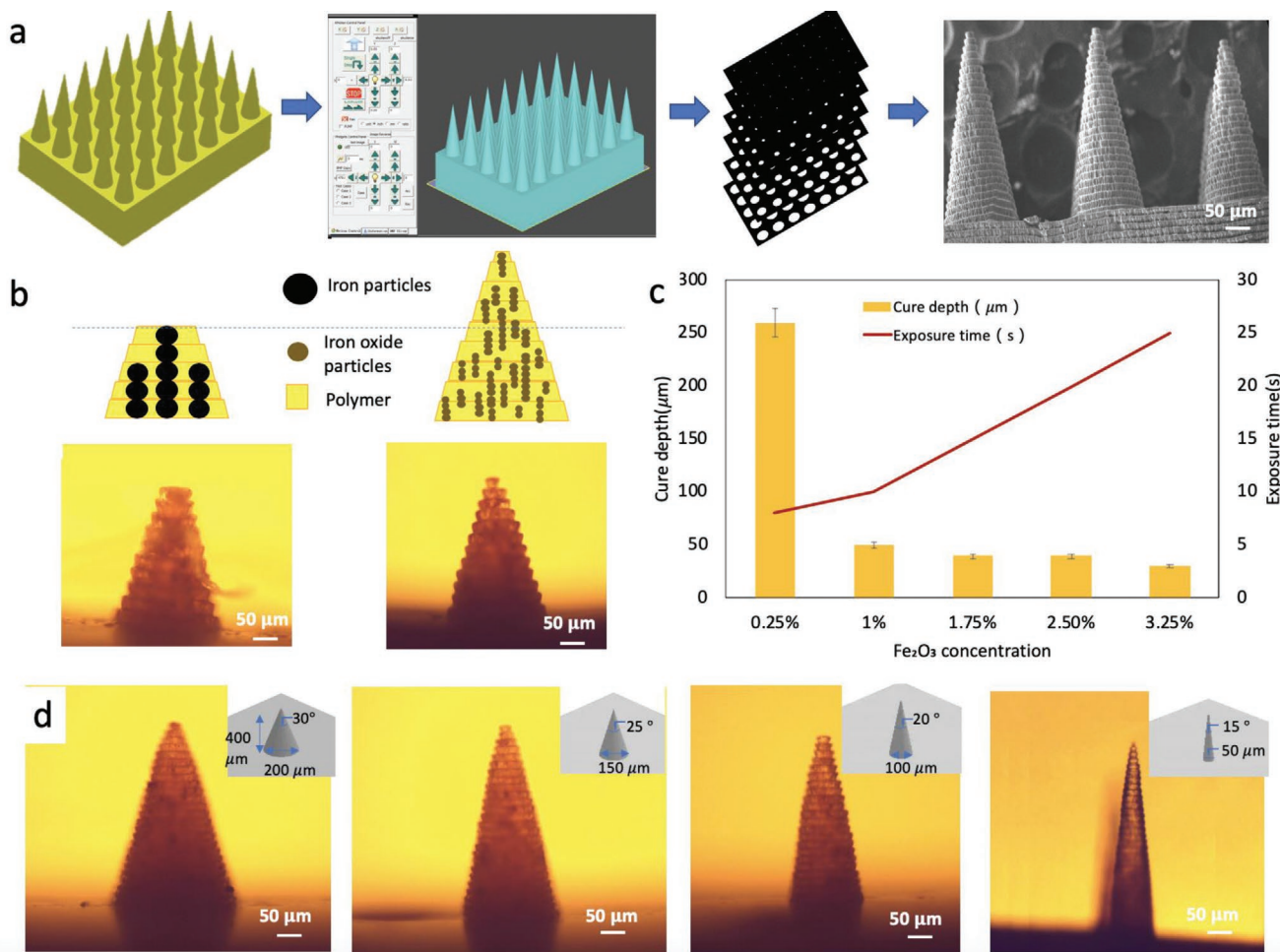


Figure 3. Schematic diagram of the MF-3DP process for printing limpet tooth-inspired MNs. a) Digital model of MN array designed in Solidworks (left) was sliced in mask image projection-based stereolithography (MIP-SL) software (second from left) to create 2D masks (second from right). SEM image of a side view of the printed MNs (right); b) the effect of the diameter of the magnetic particles on the printing resolution of the MF-3DP process; c) the curing characteristics (layer thickness and curing time) of composite materials with different IO concentrations in the MF-3DP process; and d) the design and fabrication results of MNs with different apex angles using IO/polymer composite.

ρ' and ρ are density of resin with and without magnetic particles, respectively; I_0 is the light intensity of the light beam; and R is the radius of the light beam.

As shown in Figure 3c, the cure depth of material C_d decreased as the magnetic particle concentration w increased. Meanwhile, the exposure time increased along with the concentration of magnetic particles in the composite material. For example, the cure depth of IO/polymer composite reduced sharply from 260 to 30 μm when the IO concentration was increased by 3%. Using a 2D patterned light beam with the same light intensity, the exposure time required to solidify the resin was five times longer than the time needed to solidify pure polymer resin into the same pattern. As shown in Figure 3d, MNs with different apex angles were fabricated to study the effect of apex angles on artificial skin insertion, comparing 2.5% (w/w) IO/polymer composite (Figure 3d) to pure polymer (Figure S3, Supporting Information). Since the cross-sectional area of MNs was gradually reduced in the printing direction, the intensity of the light beam was reduced dramatically. To achieve precise fabrication, the exposure time had to

be adjusted dynamically based on the exposure area of light beam.^[24] The tip of the MN printed with MF-3DP was as small as 8 μm, which is crucial because the sharpness of such a fine tip can greatly reduce the pain experienced during insertion (Figure S4, Supporting Information).

2.3. Investigation of Reinforcement Mechanisms

Limpet teeth are extremely strong due to their incorporation of regularly arranged internal mineral fillers. By aligning IOs in the magnetic field, we improved the mechanical performance of 3D-printed MNs with aIO composite, which can be attributed to the aIO microbundles encapsulated by the polymer matrix. As shown in Figure 4a, the ratio of diameter d to height H of the printed MNs ranged from 1: 50 (tip) to 1: 8 (bottom). Elastic buckling occurred and further extended over the entire polymer-based MN after the tip was subjected to a gradually increasing load.^[43] This is because the load reached the critical level of buckling force F_c , which can be calculated by

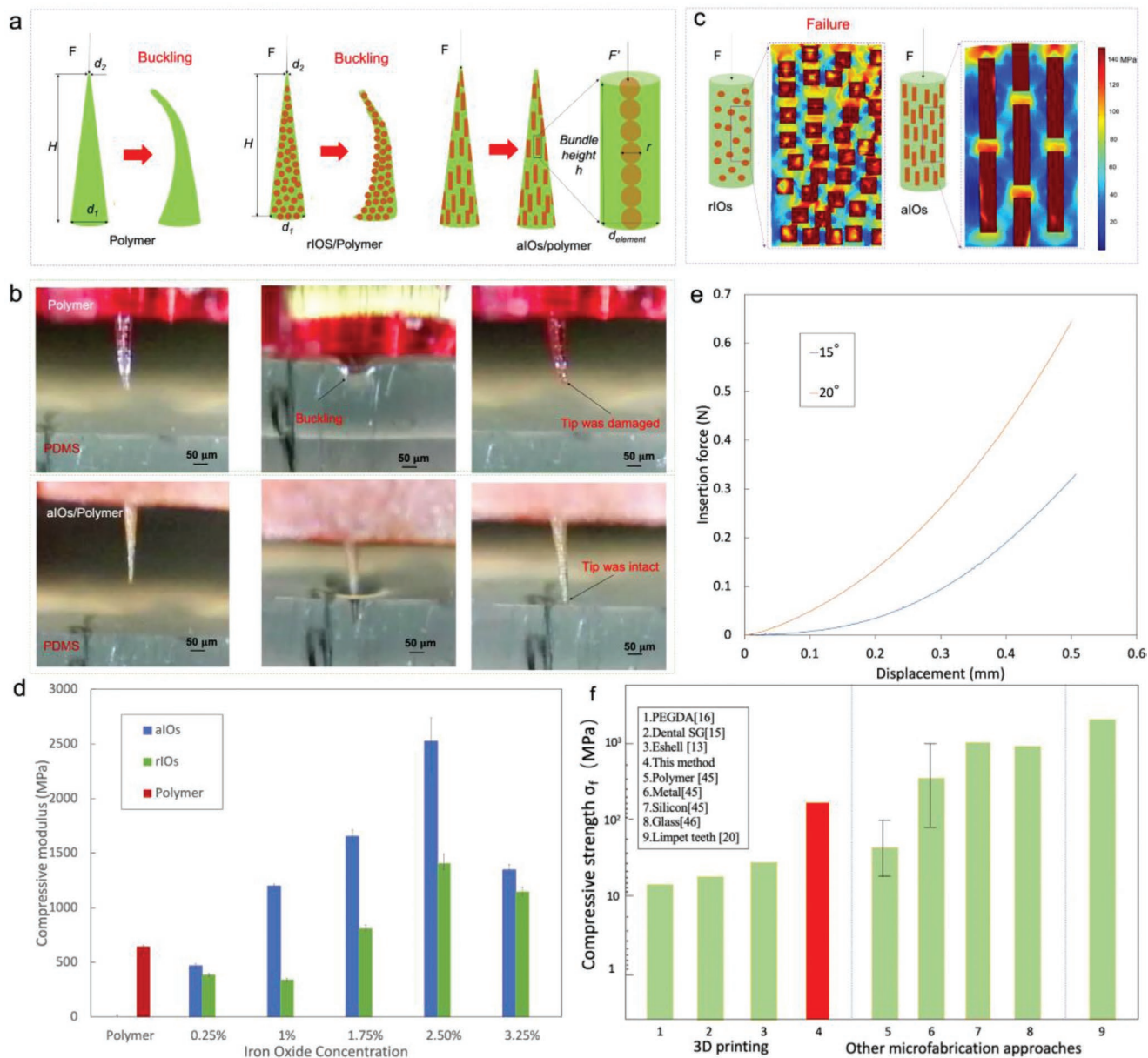


Figure 4. Mechanical performance and insertion testing of the MF-3D-printed MNs. a) Schematic diagram of shape deformation of MNs with pure polymer, rIOs and aIOs when a compression load is applied; b) insertion of MNs made of pure polymer (left) and aIOs/polymer (right) into artificial skin; c) simulations of the stress distribution of rIOs/polymer and aIOs/polymer after applying a compression force; d) comparison of the compressive modulus of the MF-3D-printed material with different IO concentrations; e) the insertion forces of aIO/polymer-based MNs with different apex angles when the MNs pierced the artificial skin; and f) compressive strength of the 3D printed limpet teeth inspired 2.5% aIOs composite with others' work.

$$F_c = \frac{n^2 \pi^2 E I_0 \left(\frac{2Hd_2}{d_1 - d_2} \right)^2}{\left(\frac{2Hd_1}{d_1 - d_2} \right)^2 H^2} = \frac{n^2 \pi^2 E d_2^2 \frac{1}{4} \pi \left(\frac{d_1}{2} \right)^4}{d_1^2 H^2} = \frac{n^2 \pi^3 E d_1^2 d_2^2}{64 H^2} = \frac{\beta E d_1^2 d_2^2}{H^2} \quad (4)$$

where E is the compressive modulus, I is the area moment of inertia, β is constant value, d_1 and d_2 are the bottom and top diameters of the MN, and H is the effective height.^[44] Given the minimum insertion force F_I , the maximum height

of MN without buckling can be calculated by the following equation:

$$H_m = \sqrt{\frac{\beta E d_1^2 d_2^2}{F_I}} \quad (5)$$

The theoretical maximum height h of MNs in aligned 2.5% iron oxide composite material under the insertion force ($F = 0.35$ N) without buckling increased to 591.09 μm which is larger than the design height 500 μm . However, the same design height of MNs in polymer is much larger than the

theoretical maximum height h , which is only 298.32 μm . As a result, the 2.5% aIOs composite MN could pierce artificial skin without buckling, but the pure polymer MN buckled during the insertion (Figure 4b). The theoretical maximum height h of MNs made by different material without buckling was shown in Figure S5, Supporting Information. Similar buckling happens in rIO-based MNs even with an increased E due to the iron oxide nanoparticles distributed in the MN structure (refer to Figure S5, Supporting Information).

Furthermore, a structural simulation using COMSOL Multiphysics showed that the deformation experienced by rIO-based composite would be greater than that of aIO-based composite under the same load, and the stress on the polymer of the rIO-based composite would cause a critical failure (Figure 4c). In the aIO-based composite, the stress was loaded on the top and bottom of the joint area between the aIOs and the polymer, and the stress on the polymer, which more easily fails, was at a relatively low level during the compression (Figure 4c). The compressive maximum load and modulus of 3D-printed structures with rIOs and aIOs as well as pure polymer were studied by conducting physical compression tests. The results showed that the compressive modulus of 2.5 wt% aIO-based composite was 4 times and 1.79 times that of pure polymer and rIO-based composite, respectively (Figure 4d). The elastic-plastic response of MF-3D-printed aIOs-based composite is shown in Figure S6a, Supporting Information, and both the maximum compressive load and modulus reached their peak values when the IO concentration was 2.5% (w/w). However, the corresponding mechanical indices of 3.25% (w/w) aIO-based composite were lower, resulting from the light scattering due to the nanoparticle aggregation and lower crosslink ratio of polymer during light projection. Both the simulation and physical tests showed that the composite material with bioinspired particle alignment had dramatically improved compression performance. However, in terms of toughness, there was no significant effect of the alignment of IOs on the performance. This is because the IOs were assembled into microbundles in the magnetic field and fixed by the photocured polymer during the printing process. Upon the removal of the magnetic field, the magnetic forces between the aIOs mostly disappeared. Consequently, the reinforcement of aIOs only exists for the compression in the microbundle direction. When a bending force was applied to the 3D-printed aIO and rIO composite structures, there was no significant difference in their fracture toughness K_{Ic} (Figure S7, Supporting Information).

To demonstrate the enhanced compression performance of the aIO-based material, we inserted MF-3D-printed MNs fabricated from pure polymer and IO/polymer composites into artificial skin (Video s2, Supporting Information, and Figure 4b). The bottom diameter of each 3D-printed MN was 50 μm , which should be small enough to result in painless insertion based on previous findings, if the MNs have sufficient strength to retain their shape. As shown in Figure 4b, the pure polymer-based MNs buckled when they were inserted into the polydimethylsiloxane (PDMS) artificial skin (with similar modulus as human skin), and the tip was damaged during the insertion due to their poor mechanical performance. Even when the bottom diameter of the polymer-based MNs was increased to 200 μm , the tip

was still not able to remain intact upon insertion (Figure S8, Supporting Information). In contrast, when reinforced with aIOs in the polymer matrix, the MF-3D-printed MNs with a 50 μm bottom diameter were able to pierce the PDMS with a force of 0.35 N (Figure 4e), and the tips of aIO/polymer-based MNs remained intact after multiple insertions (Figure 4b). The external insertion load was transferred to the high Young's modulus aIO bundles instead of the polymer, making the MNs less prone to buckle. As shown in Figure 4f, the compressive strength of the MF-3D-printed aIO-based material is more than 5 times that of other 3D printed MNs.^[13,15,16,45,46]

2.4. Investigation of Insertion-Related Pain

The pain associated with the insertion of MF-3D-printed MNs is difficult to quantify. We used a mouse model to qualitatively analyze insertion pain by evaluating "pain-like" behaviors.^[47,48] Mouse skin, which is 10 times thinner than human skin, is approximately 200 μm thick.^[49] Accordingly, 3×2 arrays of MNs were printed from aIO-reinforced polymer using the MF-3DP process. Biocompatibility testing was conducted and confirmed that the material did not significantly affect the viability of cells in vitro (Figure S9, Supporting Information). The MNs were inserted into the mouse skin by applying light pressure with a finger (Figure 5a). After the MNs were removed from the mouse skin, small holes were observed in the skin, and they disappeared soon after the neighboring tissues recovered. The tips of the MF-3D-printed MNs with aIO bundles were observed to remain in good condition after multiple insertions (Figure 5b). The behaviors of mice that wore the MF-3D-printed MN patch were compared to controls without a patch. There were no obvious behavioral differences between the mice with and without the patch (Figure 5c and Video S3, Supporting Information). We did not observe any typical pain-associated behavioral changes,^[47,48] such as rapid breathing, aggression, restlessness, or self-isolation, during our long-term observation of mice wearing the MF-3D-printed MN patch (see Video S3, Supporting Information).

We suspect that mice did not feel the presence of the MNs, as they did not paw or sniff the area where the MF-3D-printed MNs were inserted (see Video S3, Supporting Information). The MF-3D-printed MNs did not cause any observable changes to the daily activities or activity levels of the mice compared to controls. The MF-3DP process enabled the fabrication of MNs with sharp tips as well as good mechanical performance, enabling this unobtrusive, painless patch wear. Our newly developed process allowed us to reduce the diameter and increase the length of MNs while still preventing them from buckling during insertion. Like the proboscis of a mosquito, a needle with this long and thin shape can pierce the skin without being noticed, while the probe is able to remain firmly in the skin regardless of disturbance due to normal activities.^[50] The in vivo testing on mouse skin confirmed these advantages of MF-3D-printed MNs, which can remain firmly attached yet comfortable during prolonged periods of usage.

In addition to these characteristics, it is crucial for MNs to enable controllable drug delivery if they are to be widely adopted for biomedical applications.^[2-4,8] The skin of swine is typically

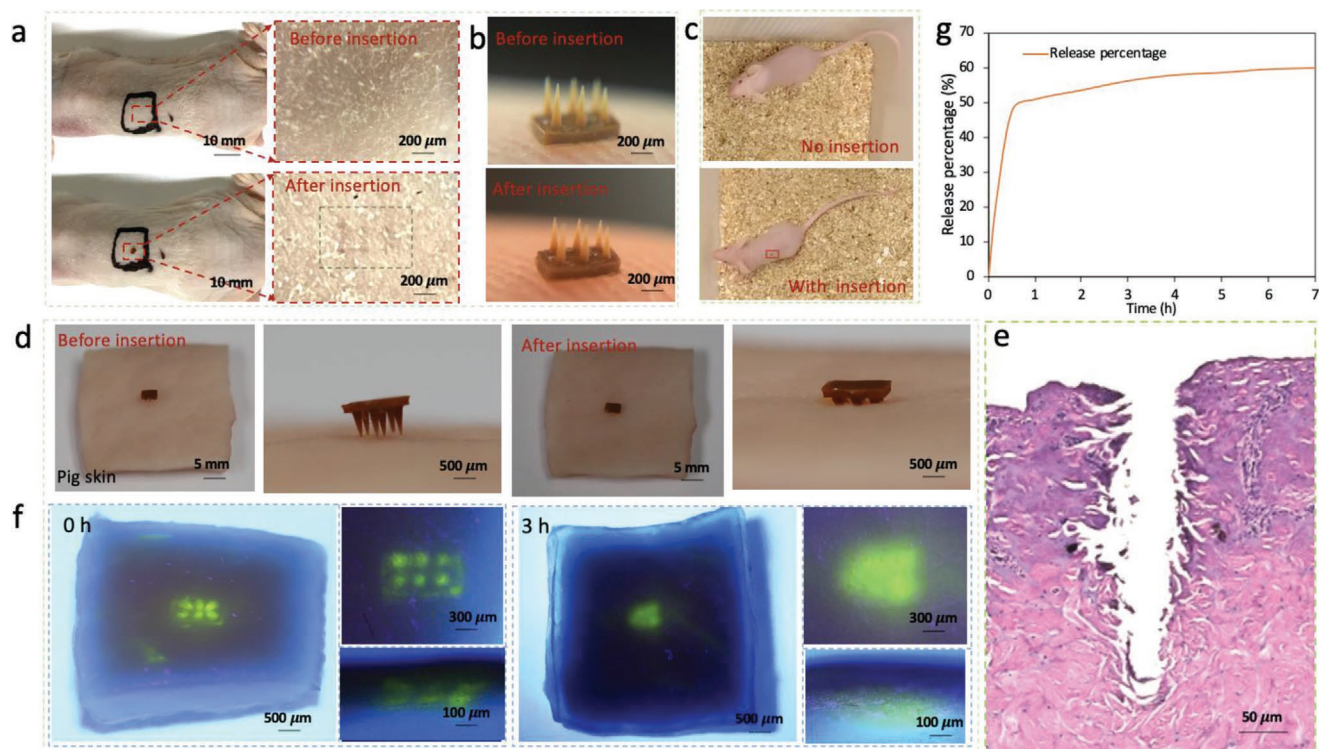


Figure 5. Dermal insertion of MF-3D-printed MNs with aIO reinforcement. a) Optical microscopy images of mouse skin before and after the insertion of MNs; b) optical microscopy images of MF-3D-printed MNs with aIO reinforcement before and after insertion; c) control mouse (top) and mouse wearing patch of MF-3D-printed MNs (bottom); d) optical microscopy images of porcine skin before and after the insertion of MF-3D-printed MNs; e) H&E stain analysis of porcine skin after the insertion of MNs; f) optical microscopy images of fluorescein release inside porcine skin 0 and 3 h after insertion of the fluorescein-coated MF-3D-printed MNs; and g) the cumulative release of Rho-B from MF-3D-printed MNs coated with Rho-B over time.

used as a large animal pre-clinical model because its thickness and other properties are relatively close to those of human skin. Therefore, the drug release of MF-3D-printed MNs with aIO reinforcement was investigated using porcine skin. The MNs were inserted into fresh porcine skin (Figure 5d), and hematoxylin and eosin (H&E) staining indicated that the MF-3D-printed MNs pierced the dermal layer (Figure 5e). To assess the drug release mechanism, fluorescein-coated MNs were inserted into fresh porcine skin. After the MNs were removed, as shown in Figure 5f, fluorescence was primarily detected at the insertion sites of the MNs, after which the fluorescein homogeneously diffused quickly inside the tissue. After 3 h, the depth of fluorescein penetration was 3 times greater than the initial post-insertion value. The release distribution of fluorescein inside the porcine skin over time is shown in detail in Figure S10, Supporting Information. Additionally, Rhodamine B (Rho-B) was used to coat the MF-3D-printed MNs and its release kinetics were assessed in vitro. The cumulative drug release from MF-3D-printed MNs is shown in Figure 5g. The release speed of Rho-B increased dramatically in the first hour until the percentage of the drug in the medium approached 50%. After that, the release slowed rapidly, and the remaining 50% of Rho-B was gradually released from the MF-3D-printed MNs over the course of two days. Overall, our studies showed that the MF-3DP process provides a potential tool for the fabrication of MNs with sharp and tiny features at precise shape

control as well as desired mechanical integrity, and the geometric morphology of MNs can be further explored to modulate their properties for controlled drug delivery in the future.

4. Conclusion

In summary, the lessons learned from limpet teeth provide the inspiration for designing microstructures with high mechanical strength. Here, we describe a MF-3DP process that we developed to fabricate MNs with hierarchical, limpet tooth-inspired, aIO-reinforced composite architectures. The 3D-printed MNs with aIOs show enhanced compression resistance and mechanical integrity due to the synergistic effect. The alignment of IOs led to anisotropic mechanical properties, enabling the fabrication of MNs with sharp and long features as well as strong mechanical performance. We demonstrated that aIO bundle-based microfillers, which are essential for withstanding the compressive force loading on the 3D-printed MNs during dermal insertion, can be assembled by applying a magnetic field during the printing process. The mechanical performance of the MNs can be tuned by altering the density and diameter of the aIO bundles, parameters which are in turn controlled by both the IO concentration in the polymer composite and the intensity of the magnetic field. This newly developed MF-3DP process provides a new way to fabricate microstructures with

excellent mechanical properties as well as high precision. Animal studies demonstrated that the MF-3D-printed MNs with aIOs can be painlessly inserted and achieve controllable drug release. The MF-3DP process opens up intriguing new avenues for designing high-compression-strength MNs using ultra-tiny bioinspired features in customized configurations. We believe that this work will be helpful to promote the adoption of 3D-printed MNs for broad biomedical and clinical applications in the future.

3. Experimental Section

Preparation of Iron/Iron Oxide Composite Resin: Photocurable Eglass resin (purchased from EnvisionTEC Inc.) was used to fabricate MNs due to its high photosensitivity. Oil Red (0.1 wt%) was added to the Eglass resin to control the curing depth of the material. The mixture was stirred for 2 h and then placed in an ultrasonic bath for 30 min to uniformly disperse the oil red powder inside the resin. Different mass ratios (5, 10, 15, 20, and 25 wt%) of carbonyl iron micro particles (purchased from Sigma Aldrich) with particle size 3–5 μm were mixed with the Eglass resin using the above method. Different mass ratios (0.25, 1, 1.75, 2.5, and 3.25 wt%) of iron oxide nanoparticles (purchased from Sigma Aldrich) with particle sizes smaller than 50 nm were mixed with the Eglass resin using the same method. All solutions were degassed under a vacuum before fabrication to remove air bubbles.

MF-3DP of MNs: In the MF-3DP process, the photocurable material was deposited on the surface of a transparent resin tank layer by layer, and each layer of the photocurable material was selectively cured to form a solid pattern when a 2D light beam was projected from the bottom optical system (Figure 2a).^[51] To generate the 2D patterned light beam, 405 nm wavelength light was reflected by a digital micromirror device (DMD) comprised of a 1920×1080 array of micromirrors, and the brightness of each pixel in the projected light beam was controlled by adjusting the angle of the corresponding micromirror in the DMD.^[52] The reflected light was further focused by an achromatic objective lens (purchased from Thorlabs Inc.) with focus distance $f = 15$ mm, and the resolution of the projected light beam was $2.5 \mu\text{m pixel}^{-1}$ (Figure 2a).^[53] A magnetic ring ($1.02'' \times 0.75'' \times 0.125''$) was placed beyond the material tank to generate a circular magnetic field (Figure 2a), so that the IOs in the IO/polymer composite formed aligned microbundles in the printing direction within each printed layer. To study the effect of the geometric morphology of MNs on the insertion of artificial skin, MNs with different geometric shapes were created using SolidWorks (see in Figure S3, Supporting Information). The height of each MN was 500 μm and different arrays were created with the diameters of the MNs ranging from 50 to 200 μm . The computer-generated model of the MNs was virtually sliced to generate a series of mask projection images with the slicing thickness ranging from 10 μm to 25 μm for a smooth surface (Figure 3a and Figure S4, Supporting Information).^[54] The exposure time was adjusted based on the light intensity and the photosensitivity of the printing material (ranging from 20 to 35 s) to improve the fabrication accuracy.^[53]

Simulation and Mechanical Testing: The magnetic field strength of the permanent magnet used in MF-3DP was simulated by COMSOL Multiphysics software. Firstly, the 3D model of permanent magnet (1 1/4" OD \times 3/4" ID \times 1/8" thickness) was designed by Solidworks and imported into COMSOL Multiphysics. The relative magnetic permeability of the magnet and the atmosphere was chosen to simulate the real experimental environment. The Brmax (Residual Induction) is 13 200 Gauss, and BHmax (Maximum Energy Product) is 42 MGOe. Based on the magnetism, the boundary condition was defined on the related surface, and the magnetic induction line of the generated magnetic field was formed on the given surface of the magnet and the atmosphere.

The stress distributions of pure polymer, rIOs/polymer, and aIOs/polymer were simulated by importing the Solidworks model described

above into COMSOL Multiphysics. A force of 100 N was applied to the model to study the strain-stress distribution. The moduli of the polymer and IOs were set to 600 MPa and 360 Gpa, respectively. Mechanical properties of the MF-3DP-printed material with and without rIOs and aIOs were studied using a compression machine (Instron 5492 dual column testing systems, Instron, MA, USA). Solid cylinders (3 mm \times 1.5 mm \times 1.5 mm) with and without rIOs or aIOs were fabricated using the MF-3DP process for the compression tests ($n = 3$ samples per group). Each specimen was tested by gradually increasing the load until the sample failed completely. The compressive strength σ_f of the 3D-printed material were calculated by using the follow equation:

$$\sigma_f = \frac{F_m}{A} \quad (6)$$

and compressive modulus E_c was calculated based on the stress-strain curve by using the equation:

$$E_c = \frac{FL}{A\Delta L} \quad (7)$$

where F is the load applied, F_m is the maximum compressive load, L and A are the length and section area of testing sample.

Bending tests were conducted using the same machine. Sample bars (8 \times 2 \times 1.5 mm) with a notched depth of 0.3 mm were printed by using 2.5 wt% of rIOs and aIOs composite material respectively. The samples were tested with a loading rate of 5 mm min^{-1} and the maximum compression distance was 1.5 mm. The fracture toughness K_{Ic} of 3D-printed composite with rIOs and aIOs was calculated using the following equation:^[55]

$$K_{Ic} = \frac{3(a/W)^{3/2} P_{Ic} S \left[1.99 - (a/W)(1-a/W) \left(2.15 - 3.93a/W + (a/W)^2 \right) \right]}{2BW^{3/2} (1+2a/W)(1-a/W)^{3/2}} \quad (8)$$

where a is the notch depth, W is the width of the specimen, P_{Ic} is the maximum load in the single-edge notched bending (SENB) test, S is the span of supports at both ends of the specimen, and B is the height of the specimen.

Insertion Testing with Artificial Skin: The Young's modulus of human skin is 400 kPa, so a substrate with a similar modulus, PDMS (380 kPa), was used as artificial skin for insertion testing. In this experiment, the moving speed of the linear stage to move the MNs was set to a comparatively low value of 0.1 mm s^{-1} . The transition of resistance force during insertion was detected by a load cell. A digital microscope (Dinolite, Torrance, CA) was used to record the insertion process of the MF-3D-printed MNs and a schematic diagram of the experimental setup is shown in Figure S8, Supporting Information.

Biocompatibility of MF-3D-Printed MNs Array: NIH3t3 cells were seeded at 2.5×10^4 per well in a 48-well plate and allowed to rest for 24 h for attachment. Then MF-3D-printed MNs were co-cultured with the cells to test their effect on cell proliferation.^[54] Cells were harvested at indicated time points and quantified using a cell counter following the standard protocol in ref. [54]. The result of cell number is shown in Figure S9, Supporting Information.

Animal Insertion of MF-3D-Printed MN: C57BL/6J mice at 8–10 weeks old were used in the present study. All mouse experiments were conducted in accordance with protocols approved by the Institutional Animal Care and Use Committee of the University of Southern California. Fresh porcine back skin was purchased from Sierra for Medical Science, and it was cut into small pieces (10 \times 10 mm) for the insertion test. The MF-3D-printed MN array was placed on the top surface of the porcine skin, and the back side of the MN array was pressed with one finger. After the insertion, the array was removed, and the porcine skin was dissected and fixed in 4% paraformaldehyde overnight at 4 $^{\circ}\text{C}$. Samples were passed through serial concentrations of ethanol for embedding in paraffin wax and sectioned at 10 μm using a microtome (Leica). Deparaffinized sections were stained with Hematoxylin and Eosin using standard procedures for general morphology.

In order to visualize drug release from the MF-3D-printed MNs, fluorescein was used to monitor the drug release process inside the porcine skin. Fluorescein (purchased from Sigma Aldrich) was dissolved in alcohol, and MF-3D-printed MNs array were soaked in the solution for 5 min. The MN array was then removed from the solution and air dried until the alcohol evaporated. The fluorescein-coated MN array was inserted into the porcine skin and the fluorescein diffusion was observed using a camera over time. Images of the porcine skin with the MN array were captured under UV light at different time points (Figure 5f and Figure S10, Supporting Information).

In Vitro Sustained Drug Release of Rho-B-Coated MF-3D-Printed MNs: MF-3D-printed MNs were coated in Rho-B as follows. Rho-B powder was gradually dissolved in ethanol until it reached the saturation point. The solution was stirred for 30 min and then placed in an ultrasonic bath for 30 min to ensure a uniform solution. The MF-3D-printed MNs were dip-coated in the saturated Rho-B solution. After that, the MNs were air dried for 12 h for the ethanol to evaporate.

The Rho-B-coated MF-3D-printed MNs were immersed in PBS solution in a beaker to evaluate the drug release. 200 μ L of the PBS solution with Rho-B release was taken from the beaker and added into a well of a 48-wells plate each hour within the first 8 h. Afterwards, the sample period was changed to every 6 h until reaching 48 h. During the period of 48 h, the 48-well plate was incubated at 20 °C and in the dark. Then all the Rho-B samples in different wells of the plate were measured at 542 nm on a micro-plate reader (SpectraMax iD3, molecular devices). The percentage of Rho-B in the PBS solution was calculated with reference to the control wells of pure PBS solution, which were assumed to have no Rho-B.

Supporting Information

Supporting Information is available from the Wiley Online Library or from the author.

Acknowledgements

The authors acknowledge the funding support of the National Science Foundation (NSF) (grant nos. CMMI 1663663 and CMMI 1151191), USC's Alfred E. Mann Institute, and ASU startup funding. They also acknowledge the Core Center of Excellence in Nano Imaging (CNI) at USC for the use of microscopic measuring equipment. Finally, they would like to acknowledge Prof. Qiming Wang at USC for his suggestion on buckling analysis.

Conflict of Interest

The authors declare no conflict of interest.

Keywords

3D printing, limpet teeth, magnetic field, mechanical reinforcement, microneedles

Received: April 29, 2020
Revised: September 8, 2020
Published online:

- [1] Y. C. Kim, J. H. Park, M. R. Prausnitz, *Adv. Drug Delivery Rev.* **2012**, *64*, 1547.
[2] S. Yang, F. Wu, J. Liu, G. Fan, W. Welsh, H. Zhu, T. Jin, *Adv. Funct. Mater.* **2015**, *25*, 29.

- [3] R. F. Donnelly, T. R. R. Singh, M. J. Garland, K. Migalska, R. Majithiya, C. M. McCrudden, P. L. Kole, T. M. T. Mahmood, H. O. McCarthy, A. D. Woolfson, *Adv. Funct. Mater.* **2012**, *22*, 4879.
[4] K. Tsiaris, W. K. Raja, E. M. Pritchard, B. Panilaitis, D. L. Kaplan, F. G. Omenetto, *Adv. Funct. Mater.* **2012**, *22*, 330.
[5] A. R. Johnson, C. L. Caudill, J. R. Tumbleston, C. J. Bloomquist, K. A. Moga, A. Ermoshkin, D. Shirvanyants, S. J. Mecham, J. C. Luft, J. M. DeSimone, *PLoS One* **2016**, *11*, 9.
[6] H. S. Gill, D. D. Denson, B. A. Burris, M. R. Prausnitz, *The Clinical Journal of Pain* **2008**, *24*, 585.
[7] S. Chen, H. Matsumoto, Y. Moro-oka, M. Tanaka, Y. Miyahara, T. Suganami, A. Matsumoto, *Adv. Funct. Mater.* **2019**, *29*, 7.
[8] M. A. Luzuriaga, D. R. Berry, J. C. Reagan, R. A. Smaldone, J. J. Gassensmith, *Lab Chip* **2018**, *18*, 1223.
[9] Y. S. Leung, T. H. Kwok, X. Li, Y. Yang, C. C. Wang, Y. Chen, *J. Comput. Inf. Sci. Eng.* **2019**, *19*, 2.
[10] Y. Yang, X. Song, X. Li, Z. Chen, C. Zhou, Q. Zhou, Y. Chen, *Adv. Mater.* **2018**, *30*, 36.
[11] D. Han, R. S. Morde, S. Mariani, A. A. La Mattina, E. Vignali, C. Yang, G. Barillaro, H. Lee, *Adv. Funct. Mater.* **2020**, *30*, 11.
[12] S. D. Gittard, A. Ovsianikov, N. A. Monteiro-Riviere, J. Lusk, P. Morel, P. Minghetti, C. Lenardi, B. N. Chichkov, R. J. Narayan, *J. Diabetes Sci. Technol.* **2009**, *3*, 304.
[13] S. D. Gittard, P. R. Miller, C. Jin, T. N. Martin, R. D. Boehm, B. J. Chisholm, S. J. Stafslin, J. W. Daniels, N. Cilz, N. A. Monteiro-Riviere, A. Nasir, *Jom* **2011**, *63*, 59.
[14] S. D. Gittard, A. Ovsianikov, H. Akar, B. Chichkov, N. A. Monteiro-Riviere, S. Stafslin, B. Chisholm, C. C. Shin, C. M. Shih, S. J. Lin, Y. Y. Su, *Adv. Eng. Mater.* **2010**, *12*, 4.
[15] C. P. P. Pere, S. N. Economidou, G. Lall, C. Ziraud, J. S. Boateng, B. D. Alexander, D. A. Lamprou, D. Douroumis, *Int. J. Pharm.* **2018**, *544*, 425.
[16] Z. Ali, E. B. Türeyen, Y. Karpat, M. Çakmakçı, *Procedia CIRP* **2016**, *42*, 87.
[17] S. H. Lim, J. Y. Ng, L. Kang, *Biofabrication* **2017**, *9*, 015010.
[18] M. Ochoa, J. Zhou, R. Rahimi, V. Badwaik, D. Thompson, B. Ziaie, in *2015 Transducers-2015 18th Int. Conf. Solid-State Sensors, Actuators and Microsystems (TRANSDUCERS)*, IEEE, Piscataway, NJ **2015**.
[19] T. N. Tarbox, A. B. Watts, Z. Cui, R. O. Williams, *Drug Delivery Transl. Res.* **2018**, *8*, 1828.
[20] A. H. Barber, D. Lu, N. M. Pugno, *J. R. Soc. Interface* **2015**, *12*, 20141326.
[21] Y. Yang, X. Li, M. Chu, H. Sun, J. Jin, K. Yu, Q. Wang, Q. Zhou, Y. Chen, *Sci. Adv.* **2019**, *5*, 4.
[22] Y. Yang, Z. Chen, X. Song, Z. Zhang, J. Zhang, K. K. Shung, Q. Zhou, Y. Chen, *Adv. Mater.* **2019**, *29*, 11.
[23] X. Li, Y. Yang, L. Liu, Y. Chen, M. Chu, H. Sun, W. Shan, Y. Chen, *Adv. Mater. Interfaces* **2020**, *7*, 3.
[24] Y. Yang, X. Li, X. Zheng, Z. Chen, Q. Zhou, Y. Chen, *Adv. Mater.* **2018**, *30*, 9.
[25] X. Li, Y. Chen, in *Proc. Int. Symp. Flexible Automation*, The Institute of Systems, Control and Information Engineers, **2018**.
[26] R. W. Dehn, P. Asprey, *Essential Clinical Procedures*, Elsevier Health Sciences, Oxford **2013**.
[27] J. A. Mikszta, J. P. Dekker, N. G. Harvey, C. H. Dean, J. M. Brittingham, J. Huang, V. J. Sullivan, B. Dyas, C. J. Roy, R. G. Ulrich, *Infect. Immun.* **2016**, *74*, 12.
[28] L. Lu, P. Guo, Y. Pan, *J. Manuf. Sci. Eng.* **2017**, *139*, 7.
[29] J. J. Martin, B. E. Fiore, R. M. Erb, *Nat. Commun.* **2015**, *6*, 1.
[30] N. M. Pugno, S. W. Cranford, M. J. Buehler, *Small* **2013**, *9*, 2747.
[31] F. L. Bargardi, H. Le Ferrand, R. Libanori, A. R. Studart, *Nat. Commun.* **2016**, *7*, 13912.
[32] Y. Kim, H. Yuk, R. Zhao, S. A. Chester, X. Zhao, *Nature* **2018**, *558*, 274.

- [33] J. Yu, B. Wang, X. Du, Q. Wang, L. Zhang, *Nat. Commun.* **2018**, 9, 1.
- [34] J. M. Camacho, V. Sosa, *Rev. Mex. Fís. E* **2013**, 59, 8.
- [35] Q. Cao, X. Han, L. Li, *Lab Chip* **2014**, 14, 2762.
- [36] Y. Sahoo, M. Cheon, S. Wang, H. Luo, E. P. Furlani, P. N. Prasad, *J. Phys. Chem. B* **2004**, 108, 3380.
- [37] P. J. Krommenhoek, J. B. Tracy, *Part. Part. Syst. Char.* **2013**, 30, 759.
- [38] J. B. Tracy, T. M. Crawford, *MRS Bull.* **2013**, 38, 11.
- [39] P. F. Jacobs, *Rapid Prototyping & Manufacturing: Fundamentals of Stereolithography*. Society of Manufacturing Engineers **1992**.
- [40] J. H. Lee, R. K. Prud'Homme, I. A. Aksay, *J. Mater. Res.* **2001**, 16, 12.
- [41] M. Yasui, K. Ikuta, *Microsyst. Nanoeng.* **2017**, 3, 1.
- [42] Y. Abouliatim, T. Chartier, P. Abelard, C. Chaput, C. Delage, *J. Eur. Ceram. Soc.* **2009**, 29, 919.
- [43] A. R. Champneys, G. W. Hunt, J. M. T. Thompson, *Localization and Solitary Waves in Solid Mechanics*, Vol. 12, World Scientific **1999**.
- [44] E. C. Zeeman, *Euler Buckling*, Springer, Berlin, Heidelberg **1976**.
- [45] K. Ita, *Pharmaceutics* **2015**, 7, 90.
- [46] H. Juster, B. van der Aar, H. de Brouwer, *Polym. Eng. & Sci.* **2019**, 59, 5.
- [47] National Research Council, *Recognition and Alleviation of Pain in Laboratory Animals*, National Academies Press, Washington DC **2010**.
- [48] J. R. Deuis, L. S. Dvorakova, I. Vetter, *Front. Mol. Neurosci.* **2017**, 10.
- [49] J. C. Wei, G. A. Edwards, D. J. Martin, H. Huang, M. L. Crichton, M. A. Kendall, *Sci. Rep.* **2017**, 7, 1.
- [50] X. Q. Kong, C. W. Wu, *Phys. Rev. E* **2010**, 82, 011910.
- [51] X. Li, Y. Yang, B. Xie, M. Chu, H. Sun, S. Hao, Y. Chen, Y. Chen, *Adv. Mater. Technol.* **2019**, 4, 2.
- [52] X. Li, T. Baldacchin, X. Song, Y. Chen, in *The 11th Int. Conf. Micro Manufacturing (ICOMM)*, **2016**.
- [53] X. Li, Y. Chen, *J. Manuf. Processes* **2017**, 28.
- [54] X. Li, Y. Yuan, L. Liu, Y. S. Leung, Y. Chen, Y. Guo, Y. Chai, Y. Chen, *Bio-Design Manufact.* **2020**, 3, 15.
- [55] ASTM E1820-01, *Standard Test Method for Measurement of Fracture Toughness*, ASTM International, West Conshohocken, PA **2001**, www.astm.org.